



Title	Role of Specific Humidity Anomalies in Caribbean SST Response to ENSO
Author(s)	CHIKAMOTO, Yoshimitsu; TANIMOTO, Youichi
Citation	Journal of the Meteorological Society of Japan, 83(6), 959-975 https://doi.org/10.2151/jmsj.83.959
Issue Date	2005-12-26
Doc URL	http://hdl.handle.net/2115/14528
Type	article
File Information	chika_jmsj05.pdf



[Instructions for use](#)

Role of specific humidity anomalies in Caribbean SST response to ENSO

YOSHIMITSU CHIKAMOTO

Graduate School of Environmental Earth Science, Hokkaido University, Sapporo, Japan

YOUICHI TANIMOTO

Faculty of Environmental Earth Science, Hokkaido University, Sapporo, Japan

(Received 6 April 2005; revised 25 July 2005; final 19 August 2005)

Yoshimitsu Chikamoto, Graduate School of Environmental Earth Science, Hokkaido University, N10W5, Kita-ku, Sapporo, 060-0810, Japan.

E-mail: chika44@ees.hokudai.ac.jp

ABSTRACT

Remote influences of El Niño-Southern Oscillation (ENSO) on tropical Atlantic sea surface temperature (SST) are examined using reanalysis and in-situ observational datasets. During both the warm and cold events of ENSO, latent heat flux anomalies are the major mechanism for SST anomalies over the Caribbean Sea. Results from a linear decomposition of the latent heat flux anomalies indicate that the anomalous air-sea difference in specific humidity ($\Delta q'$) is the dominant term in January, one month after the ENSO's mature phase. Since anomalies of SST and saturation specific humidity at the sea surface are still small in January, $\Delta q'$ is due mostly to changes in specific humidity in the lower atmosphere. Changes in surface air humidity and temperature and their relationship to temperature variability in the upper troposphere during ENSO warm events are discussed.

1. Introduction

Sea surface temperature anomalies (SSTAs) in the northern tropical Atlantic (NTA) play an important role in pan-Atlantic climate variabilities because SSTA distribution in this region changes the meridional location of the Atlantic inter-tropical convergence zone (e.g., the review of Xie and Carton 2004). On interannual and decadal timescales, several mechanisms are involved in the tropical Atlantic SST variability: Atlantic Niño (Zebiak 1993; Sutton et al. 2000; Okumura and Xie 2004) and pan-Atlantic decadal oscillation (Xie and Tanimoto 1998; Rajagopalan et al. 1998; Tanimoto and Xie 1999; Tourre et al. 1999; Okumura et al. 2001). In addition to these mechanisms seen in the tropical Atlantic, remote influences of El Niño-Southern Oscillation (ENSO) are shown by previous observational studies. While ENSO warm (cold) events tend to be mature in boreal winters, positive (negative) SSTAs in the NTA region are formed in the boreal spring-summer season, a few months later, after the mature phase of the events in the tropical Pacific (Curtis and Hastenrath 1995; Klein et al. 1999). The ENSO index explains 20-30% of the total SST variance in the boreal spring-summer season over the NTA region (Enfield and Mayer 1997; Liu et al. 2004).

Observational studies showed that these boreal spring SSTAs in the NTA region are mainly formed by the preceding surface latent heat flux variabilities as a remote response to ENSO (Curtis and Hastenrath 1995; Klein et al. 1999). During the mature phase of the ENSO warm (cold) events, the sea level pressure anomalies tend to be positive (negative) over the equatorial Atlantic and negative (positive) over the subtropical North Atlantic (Giannini et al. 2000; Wang 2002), which reduce (enhance) the meridional pressure gradient and weaken (strengthen) the climatological northeasterly trades. These weakened

(strengthened) northeasterly trades in boreal winter reduce (enhance) latent heat release from the ocean surface and lead to warm (cold) SSTAs in the boreal spring. These anomalous surface winds and associated latent heat release over the NTA region are reproduced by the remote response to tropical Pacific SST variabilities in the atmospheric general circulation model (AGCM) experiments coupled with the slab ocean mixed layer model (Lau and Nath 2001; Alexander and Scott 2002). Huang et al. (2002), using the locally coupled atmosphere-ocean GCM only in the Atlantic sector, suggested that initial changes in the boreal winter surface wind in the NTA region during the mature phase of the ENSO events maintain SSTAs via wind-evaporation-SST feedback (Xie and Philander 1994).

In contrast, Saravanan and Chang (2000) showed that not only anomalous surface wind but also anomalous air-sea temperature differences are crucial in determining the surface heat flux anomalies in the NTA region during the mature phase of the ENSO events. They conducted two AGCM experiments: one forced by the prescribed SSTAs in the entire tropical ocean and the other by those only in the tropical Atlantic. From difference fields of these two experiments, they estimated each of the contributions from the anomalous surface wind speed (W') and the anomalous air-sea temperature difference ($\Delta T'$) to the surface turbulent heat flux anomalies (F'_{est} ; sum of latent and sensible heat flux anomalies) by linearizing the aerodynamic bulk formula as follows:

$$F'_{est} = cW'\Delta\bar{T} + c\bar{W}\Delta T', \quad (1)$$

where c is a constant coefficient evaluated from the climatological means of the surface turbulent heat flux, wind speed (\bar{W}), and air-sea temperature difference ($\Delta\bar{T}$). In their model, regressed anomalies of the first and second terms on the right-hand side onto the Niño3 index showed comparable contributions to surface turbulent heat flux anomalies in

the NTA region after the mature phase of the ENSO events.

Chiang and Sobel (2002) proposed a mechanism of the tropical tropospheric response to the ENSO events (hereafter TT-mechanism) applying the strict quasi-equilibrium (SQE) concept (Emanuel et al. 1994). Under the SQE, the equivalent potential temperature in the boundary layer is related to the thermal structure in the free atmosphere so that the convective available potential energy (CAPE) is conserved over the deep convective region. In fact, Brown and Bretherton (1997) indicated that the tropospheric temperature is positively correlated with the boundary layer equivalent potential temperature over active convecting regions of the tropical oceans on a month and longer timescales. Since tropical atmosphere can not maintain zonal gradients in temperature and pressure under the weak Coriolis force, the large-scale dynamics induce zonally uniform temperature anomalies over most of the tropical belt (Charney 1963; Wallace 1992; Sobel et al. 2002). Therefore, tropospheric warming associated with the ENSO warm events is found over the most of tropical oceans (Yulaeva and Wallace 1994; Sobel et al. 2002; Chiang and Sobel 2002), thereby increasing potential temperature in the boundary layer. These increases of temperature and humidity affect underlying SSTAs via changes in turbulent heat fluxes. Chiang and Sobel (2002) suggest that the TT-mechanism operates over the NTA region.

Over the NTA region, turbulent heat flux anomalies are mainly contributed from latent heat flux anomalies rather than sensible heat flux anomalies (Curtis and Hastenrath 1995; Alexander and Scott 2002). Therefore, the direct estimation by air-sea differences in specific humidity (Δq), instead of temperature (Eq. (1)), provides a better estimation on the linearized components of turbulent heat flux anomalies. This is represented as

$$F'_{est} = cW'\Delta\bar{q} + c\bar{W}\Delta q'. \quad (2)$$

In this study, we examined the temporal sequence of components in Eq. (2) in the NTA region after the mature phase of the ENSO events, using monthly mean datasets, both from assimilated reanalysis data and in-situ marine meteorological observations. In Section 3, we will show that the second term on the right-hand side of Eq. (2) is much more significant than the first term in a particular month when SSTAs over the Caribbean Sea are still incoherent. In the subsequent sections, we will see that the coherent structure of the anomalous air-sea difference in specific humidity should be induced by changes in the lower atmosphere.

Due to the zonal asymmetry in mean SST and its effect on the deep convection, a response of anomalous diabatic heating by ENSO and associated changes in the Walker circulation are not always symmetric between the ENSO warm and cold events. In fact, spatial patterns of rainfall anomalies over the tropical Pacific do not represent symmetric responses to ENSO's extreme phases (Hoerling et al. 1997, 2001; Deweaver and Nigam 2002). Hence, we will treat the warm and cold phases of the ENSO events separately.

The rest of this paper is organized as follows. Section 2 describes the datasets and defines the ENSO warm and cold events from the Niño3 index. In Section 3, we calculate each of the contributions of wind speed anomalies and anomalous air-sea differences in specific humidity to the total amount of the latent heat flux anomalies. In Section 4, we consider the asymmetric responses of the linearized components of the latent heat flux anomaly to the ENSO events, and discuss the formation of these anomalous air-sea differences in specific humidity based on TT-mechanism during the ENSO warm events. The results are summarized in Section 5.

2. Datasets

To capture month-to-month variations in the troposphere over the tropical Atlantic ocean

after the mature phase of the ENSO events, the monthly latent heat flux from the ocean surface (upward positive), surface net heat flux, precipitation rate, and specific humidity at 2-m height are taken from the National Centers for Environmental Prediction-National Center for Atmospheric Research (NCEP-NCAR) reanalysis (Kalnay et al. 1996) approximately on a $1.875^\circ \times 1.875^\circ$ Gaussian grid. The surface net heat flux consists of the latent, sensible, shortwave, and longwave heat fluxes taken from this dataset. Monthly surface fields of wind velocity, its speed, and pressure are obtained from the NCEP-NCAR reanalysis data on a $2.5^\circ \times 2.5^\circ$ grid. Monthly horizontal wind and specific humidity fields at eight pressure levels of this dataset are also used. The monthly SST data are obtained from the global sea ice and SST (GISST) on a $1^\circ \times 1^\circ$ grid (Folland and Parker 1995). From the linearly interpolated SST and surface pressure, a monthly saturation specific humidity at the ocean surface is calculated on a $2.5^\circ \times 2.5^\circ$ grid. We calculate air-sea differences in specific humidity on a $2.5^\circ \times 2.5^\circ$ grid between the ocean surface and 2-m height using spherical harmonic interpolation.

The surface latent heat fluxes of the reanalysis data are less reliable than other elements in the free atmosphere due to insufficient treatments of the planetary boundary layer. Therefore, we employ the $2^\circ \times 2^\circ$ monthly dataset of surface latent heat fluxes based on individual marine meteorological reports archived in the Comprehensive Ocean-Atmosphere Data Set (COADS; Woodruff et al. 1987). Although this non-assimilated data may suffer sampling errors in the region of few marine reports, ship tracks to the Panama Canal provide a sufficient number of observations in the Caribbean Sea. However, this dataset contains some missing values over the southern tropical Atlantic and the central equatorial Atlantic since satellite observations and spatial interpolation were not used. Details of the calculation procedure are described in Tanimoto and Xie (2002) and Tanimoto et al. (2003).

We calculate the monthly climatological means based on a 52-year period (1948-1999) for NCEP-NCAR reanalysis and GISST datasets, and on a 46-year period (1950-1995) for COADS. The monthly anomalies are defined as departures from the climatological mean values.

In Section 4, we will calculate a moisture budget to examine the formation of the air-sea difference in specific humidity. In reanalysis datasets, however, the moisture budget is not always conserved due to four-dimensional data assimilation (Trenberth and Guillemot 1995; Mo and Higgins 1996; Trenberth and Guillemot 1998). For this reason, we will use two datasets to conduct an accurate estimation of the moisture budget. One is the NCEP-Department of Energy Reanalysis 2 (NCEP2; Kanamitsu et al. 2002) dataset that is a modified version of NCEP-NCAR reanalysis. The other is the precipitation obtained from the Climate Prediction Center's Merged Analysis of Precipitation (CMAP; Xie and Arkin 1997) dataset on a $2.5^\circ \times 2.5^\circ$ grid. Both NCEP2 and CMAP datasets are available from January 1979 to December 1999. A monthly moisture flux is calculated from monthly variables of horizontal winds and specific humidity on pressure levels in the NCEP2 dataset. A transient component of monthly moisture flux ($\overline{q'\mathbf{V}'}$) calculated from 4 times daily of those variables was negligible over the Caribbean Sea.

To represent the magnitude of the ENSO warm and cold events in the eastern tropical Pacific, we use time series of SSTAs in the Niño3 region (5°S - 5°N , 90° - 150°W) based on GISST. This time series averaged from November through January in the following year

Fig. 1

is defined as the Niño3 index (Fig. 1). In the present study, we refer these three months as the mature phase of the ENSO events. We extract eight higher and lower events based

Table 1

on this index. The eight warm and cold events are listed in Table 1. When we use the Niño3 index based on Reynolds Reconstructed SST (Smith et al. 1996) instead of GISST,

the 1986/87 and 1987/88 events (the 1964/65 and 1967/68 events) are selected as the 9th and 8th warmest events (the 8th and 9th cold events), respectively. Including the 1986/87 warm event and the 1964/65 cold event as the additional events to our composite does not affect our results of the analyses.

3. The formation of SSTAs in the NTA region

To represent the temporal evolution of the ENSO-related SSTAs in the NTA region, we made three monthly composite maps from December to February during the ENSO warm events (Figs. 2a, 2b, and 2c). In December, no coherent structure of SSTAs appears in this region, while the tropical Pacific SSTAs are already mature (Fig. 2a). In the following January, when matured SSTAs in the tropical Pacific gradually decrease, positive SSTA regions higher than 0.2°C emerge in the southwestern parts of the Caribbean Sea and equatorial eastern Atlantic (Fig. 2b). Furthermore, in February, the former positive SSTA region expands to the entire Caribbean Sea, and the latter extends its area to 20°N along the west coast of Africa (Fig. 2c). These results indicate that SSTAs in the NTA region during the ENSO warm events begin to be formed in the January-February period. These SSTAs over the Caribbean Sea reach a local maximum in boreal summer, as shown later (Fig. 4d). In addition to these positive SSTAs, a significant negative SSTA region is observed in the Gulf of Mexico and off the east coast of North America during February (Fig. 2c).

Fig. 2

Figures 2d-f and 2g-i show the same composite maps of SSTA tendencies and surface latent heat flux anomalies, respectively. SSTA tendency in a given month is defined as the difference between the SSTA in the subsequent month and that in the previous month. In December, this tendency (Fig. 2d) is incoherent and inconsistent with the latent heat flux anomalies (Fig. 2g). In the following January, it becomes coherent in three portions of the

NTA region: the Caribbean Sea, off the west coast of Africa, and the extratropical region over the Gulf of Mexico and off the east coast of North America (Fig. 2e). Among these regions, the coherent structures of positive SSTA tendencies in the Caribbean Sea (Figs. 2e and 2f) collocate with the zonal elongated region of the anomalous latent heat flux of -15 W m^{-2} appearing in the January-February period (Figs. 2h and 2i), while sensible heat flux anomaly is less than -5 W m^{-2} in this region (not shown). As shown in the previous studies introduced in Section 1, these latent heat flux anomalies, which explain most of the turbulent heat flux anomalies, contribute in forming positive SSTAs over the NTA region in this period.

Given that SSTA tendencies of $0.2 \text{ }^\circ\text{C}/2\text{-month}$ are only due to surface latent heat flux anomalies of -15 W m^{-2} in the Caribbean region, we obtain an equivalent mixed layer depth of 100-m, comparable to an observed isothermal layer in the northern Caribbean Sea in January (Kara et al. 2003)¹. This means that surface heat flux anomaly mainly contributes to the SSTA formation on that region. SSTA tendencies off the west coast of Africa in January, on the other hand, are about $0.5 \text{ }^\circ\text{C}/2\text{-month}$, while negative latent heat flux anomalies are less than 7.5 W m^{-2} around the same region. In this case, an equivalent mixed layer corresponds to 20-m depth. The observed isothermal layer off the west coast of Africa is deeper than this equivalent mixed layer depth, implying that SSTA in this region is controlled by coastal upwelling induced by local alongshore winds (Carton and Zhou 1997). In the Gulf of Mexico and off the east coast of North America during January, the local maximum in SSTA tendencies of $-1.0 \text{ }^\circ\text{C}/2\text{-month}$ and positive latent heat flux anomalies of 15 W m^{-2} correspond to the equivalent mixed layer depth of 20-m. This underestimation

¹Kara et al. (2003) provided monthly climatologies of isothermal layer depth that is defined as the depth where water temperature has changed by an absolute temperature difference of $0.8 \text{ }^\circ\text{C}$ from the surface layer.

of equivalent mixed layer depth suggests that the other components of net surface heat flux anomalies or ocean dynamic processes contribute to the negative SSTA formation in the Gulf of Mexico and the east coast of North America. Alexander and Scott (2002) suggested that the sensible heat flux anomalies, in addition to the latent heat flux anomalies, are important in cooling ocean along the coast of North America.

Over the negative latent heat flux anomalies in the Caribbean region, we found a coherent pattern of anomalous surface southerly and southwesterly winds in January (Fig. 2h). Given that these surface winds weaken by 0.5 m s^{-1} in northeasterly climatological trade winds, the contribution of wind speed anomalies to latent heat flux anomalies is about 9.3 W m^{-2} under the climatological air-sea difference in specific humidity. However, negative latent heat flux anomalies of -15 W m^{-2} over the Caribbean region imply that changes in the air-sea difference in specific humidity are also involved in latent heat flux anomalies. Each contribution from changes in wind speed and air-sea difference in specific humidity to the latent heat flux anomaly will be estimated later.

During the ENSO cold events, coherent SSTAs over the Caribbean region appear in December, one month earlier than the warm events, extending its area northeastward with **Fig. 3** latitude (Fig. 3a). These negative SSTAs over the Caribbean region tend to be local maxima in the following January (Fig. 3b) and further extends its area to the west coast of Africa in the subsequent February (Fig. 3c). Despite differences in initial months in the SSTA formation between the ENSO warm and cold events, the spatial structures of SSTAs over the Caribbean region and off the west coast of Africa in February show similar patterns with opposite polarity of the ENSO warm events (Figs. 2c and 3c). In the Gulf of Mexico and off the east coast of North America, however, SSTAs are incoherent from December through to the following February during the ENSO cold events.

Monthly composite maps of SSTA tendencies and latent heat flux anomalies during the ENSO cold events are shown in Figs. 3d-i. As in the warm events, SSTA tendencies during the cold events are mostly explained by latent heat flux anomalies over the Caribbean Sea in the December-January period, while coherent SSTA tendencies in the other regions require other SSTA formation processes (Figs. 3d, 3e, 3g, and 3h). The anomalous surface winds during the cold events are insufficient in explaining the latent heat flux anomalies over the Caribbean region, indicating anomalous air-sea differences in specific humidity involved in latent heat flux anomalies.

The latent heat flux anomaly can be decomposed into three linearized components as in Tanimoto et al. (2003):

$$F'_{lh} = \rho c_e L_e \{ W' \overline{\Delta q} + \overline{W} \Delta q' + (W' \Delta q' - \overline{W' \Delta q'}) \} \quad (3)$$

where F'_{lh} is the latent heat flux, W is the scalar wind speed, Δq is the air-sea difference in specific humidity, ρ is the atmospheric density, c_e is the bulk coefficient, L_e is the latent heat of vaporization for water, and the overbar and prime indicate the time mean and deviation, respectively. The bulk coefficients are assumed to be constant in NCEP-NCAR reanalysis and to be dependent on scalar wind speed and static stability in COADS. However, when we linearize the surface heat flux anomalies, we ignore the dependence of the coefficients on those variables. On the right-hand side of (3), the first two terms represent contributions of the wind speed anomaly (W') and the anomalous air-sea difference in specific humidity ($\Delta q'$) to the total amount of latent heat flux anomalies, respectively. As we will show later, the last term becomes negligible.

Figures 4a-c and 4e-g show the time evolutions of individual contributions ($W' \overline{\Delta q}$, $\overline{W} \Delta q'$)

Fig. 4

to latent heat flux anomalies during the ENSO warm and cold events. Note that the vertical

axes of heat flux anomalies are reversed for easier comparison with SSTAs. As shown in Figs. 2 and 3, SSTAs over the Caribbean Sea are formed in February, and show a local maximum in boreal summer during the both phases of ENSO (solid lines in Figs. 4d and 4h). A correlation analysis shows that the Niño3 index is positively correlated with monthly SSTAs in the Caribbean Sea from February to July. These positive correlations indicate that the ENSO variability explains 20-30% of the total variance in each of months, consistent with previous results (Enfield and Mayer 1997; Liu et al. 2004). During both phases of these events, the total amount of latent heat flux anomalies averaged over the Caribbean Sea (dashed lines in Figs. 4c and 4g) is well represented by the sum of $W'\overline{\Delta q}$ and $\overline{W}\Delta q'$ components. These latent heat flux anomalies contribute to the most of the net surface heating anomaly that is a 90-degree out of phase with the SSTAs from boreal winter through summer (Figs. 4d and 4h). For the latent heat flux anomalies during the warm events, the contribution of $\Delta q'$ in January, which is three times larger than that of W' , accounts for 64% of the total latent heat flux anomaly of 18 W m^{-2} (Figs. 4a-c). These two linearized components tend to be comparable from February through to May, and counteracting to each other from June through August (Figs. 4a and 4b). This counteracting effect induces negative SST tendency during the boreal summer. During the cold events, the contributions of $\Delta q'$ are important in representing local maxima in latent heat flux anomalies in the December-January period (Fig. 4f), while contributions of W' are considerably larger from December through to the following April (Fig. 4e). From May through July, the contributions of W' are counteracting those of $\Delta q'$. These results indicate that $\Delta q'$ in January specifically plays an important role in forming latent heat flux anomalies over the Caribbean Sea during both phases of the ENSO events. Note that the contribution of $\Delta q'$ is well captured during the ENSO warm events rather than the cold events. This asymmetry between the warm and cold events will

be examined in the next section.

Fig. 5

January composite maps of the linearized components of latent heat flux anomalies during the ENSO warm events were constructed in Figs. 5a and 5b. The sum of the two linearized components (Fig. 5c) shows a zonally elongated pattern of negative (positive) anomalies extended from the Caribbean Sea off to the west coast of Africa (over the Gulf of Mexico and off the east coast of North America). These coherent anomalies are quantitatively and qualitatively consistent with the anomalous pattern of total latent heat flux anomalies (Fig. 2h). In the Caribbean Sea, the contribution of $\Delta q'$ is 20 W m^{-2} near the center of action, while the contribution of W' is only 5 W m^{-2} in the same region. These results show that $\Delta q'$ is the major contributor to latent heat flux anomalies over the Caribbean Sea in a particular month after the mature phase of the ENSO warm events.

Based on the in-situ observational data obtained from COADS, the contributions of $\Delta q'$ (Fig. 5e) are larger than those of W' (Fig. 5d) in the Caribbean Sea. The sum of these linearized components explains the most variance of the latent heat flux anomalies over the NTA region (not shown), although there are many noisy values as well as some missing values due to insufficient measurements in the central equatorial Atlantic.

Fig. 6

During the ENSO cold events, January composite maps of individual contributions to latent heat flux anomalies based on both datasets show robust structures as in the warm events (Fig. 6). These composite maps show that about half of the latent heat flux anomalies over the Caribbean Sea and the Gulf of Mexico can be explained by $\Delta q'$.

For the formation of SSTAs over the NTA region associated with the ENSO events, previous studies indicated the importance of W' to induce changes in latent heat flux (e.g., Curtis and Hastenrath 1995; Enfield and Mayer 1997; Lau and Nath 2001). However, our observational results showed that the contributions of $\Delta q'$ are necessary in forming

substantial latent heat flux anomalies. These results are consistent with the estimation from the anomalous air-sea difference in “temperature” in the AGCM experiments by Saravanan and Chang (2000).

4. Discussion

a. Asymmetric latent heat flux anomalies to the ENSO activity

To see whether the surface meteorological variables in the Caribbean Sea linearly respond to the ENSO events, we made January scatter plots of W' and $\Delta q'$ onto the Niño3 index (Figs. 7a and 7b). For the total number (51 years) of scatters, $\Delta q'$ is correlated with the index (correlation coefficient, $r=-0.49$), while W' is less correlated ($r=-0.24$). The regressed $\Delta q'$ and W' onto the Niño3 index are -0.16 g kg^{-1} and -0.17 m s^{-1} over the Caribbean Sea, inducing -5.6 W m^{-2} and -3.0 W m^{-2} of latent heat flux anomalies, respectively. As shown with the composite analysis in Section 3, correlation analysis also shows that $\Delta q'$ rather than W' contributes to form latent heat flux anomalies over the Caribbean Sea.

Fig. 7

When we examine the correlation of $\Delta q'$ during positive and negative values of the Niño3 index separately, we find the asymmetric response of $\Delta q'$ over the Caribbean Sea to the ENSO events (Fig. 7b). During years with the positive values of the Niño3 index (23 years), 15 scatters of $\Delta q'$ (65% of all positive index years) are in the lower-right quadrant, and tend to be linear with the index. Similarly, six closed scatters among eight warm events are plotted in the lower-right quadrant. During years with the negative values (28 years), on the other hand, 15 years (56% of all negative index years) are plotted over the upper-left quadrant. However, since only two closed scatters among the eight cold events are plotted in this quadrant, the linear relation of scatters onto the index is not so apparent. As a result,

$\Delta q'$ is strongly correlated with the positive Niño3 index ($r=-0.66$) rather than the negative ($r=-0.30$). The correlation coefficients of W' are less significant regardless of the sign of the index, being -0.18 and -0.33 during positive and negative Niño3 index, respectively (Fig. 7a).

In January during the positive Niño3 index, $\Delta q'$ over the Caribbean Sea is not correlated with SSTA ($r=0.14$, not shown), but strongly correlated with a specific humidity anomaly at 2-m height (q'_a) ($r=-0.67$, not shown). Scatter plots of q'_a onto the Niño3 index (Fig. 7c) show strong correlation ($r=0.71$) regardless of the sign of the index. Specifically, during the positive Niño3 index, 21 scatters among 23 years are in the upper-right quadrant, and tend to be much more linear with the index. By contrast, scatters during the negative Niño3 index are both in the upper- and lower-left quadrants, and do not show the linear relation with the index. As a result, a correlation coefficient of q'_a during the positive index is much significant ($r=0.79$). These asymmetric responses between the positive and the negative Niño3 indices may reflect asymmetry in the Niño3 SSTA; the dominant ENSO events exceeding the Niño3 SSTA of $2.0\text{ }^\circ\text{C}$ exist during the warm events but not during the cold events (Figs. 1 and 7). Since the changes in q'_a are most pronounced during the positive Niño3 index, we will examine how q'_a is formed over the Caribbean region during the warm events.

b. Changes in surface air humidity and temperature and their relationship to temperature variability in the upper troposphere during ENSO warm events

To see the horizontal structures of q'_a and $\Delta q'$, we construct composite maps of these variables in January during the ENSO warm events (Fig. 8). A tongue-like structure of positive q'_a and the same structure but with opposite polarity of $\Delta q'$ extend northeastward

Fig. 8

from the Caribbean Sea, indicating that q'_a explains most of $\Delta q'$ on that region. By contrast, these two variables show the same polarity over the equatorial Pacific because positive q'_a is induced by warm SSTAs (Kleeman et al. 2001). These different characteristics between the Atlantic and Pacific oceans imply that the positive q'_a over the Caribbean region, under small SSTAs (Fig. 2b), should be formed by atmospheric processes induced by the ENSO forcing.

Figure 9 shows the January composite map of temperature anomaly at 400 hPa during the ENSO warm events. Associated with the tongue-like structure of positive q'_a over the Caribbean region (Fig. 8a), positive temperature anomalies at 400 hPa also appear over this region extending from the eastern tropical Pacific (Fig. 9). Tropospheric mean temperature anomalies estimated from the microwave sounding unit also show the same structure over the tropics (Yulaeva and Wallace 1994; Chiang and Sobel 2002). Over the Caribbean Sea, temperature anomalies at 400 hPa show significant positive correlations with q'_a and surface air temperature anomalies in January ($r=0.74$ and 0.75 , respectively). These results imply that the temperature anomaly in the free atmosphere is closely related to the boundary layer equivalent potential temperature anomaly, which is consistent with the SQE concept (Emanuel et al. 1994; Brown and Bretherton 1997) that requires conservation of the CAPE in the troposphere.

Figure 10 shows the time evolutions of surface air temperature anomaly and SSTA (thick solid and dashed lines, respectively) over the Caribbean Sea during the ENSO warm events. The air temperature anomalies lead the SSTAs until May except for February in COADS, and show largest difference from SSTAs in January. The q'_a also exhibits the similar behavior to the surface air temperature anomaly (Fig. 4b) because a surface relative humidity generally remains constant in the tropics. Associated with these largest $\Delta T'$ and

$\Delta q'$, air temperature anomalies at 400 hPa (thin solid line in Fig. 10) also reach a maximum in January, implying that temperature warming in the free atmosphere is closely related to the surface temperature and humidity anomalies. As results, these changes in $\Delta q'$ of 0.3 g kg^{-1} and $\Delta T'$ of $0.3 \text{ }^\circ\text{C}$ induce latent heat flux anomaly of 11 W m^{-2} and sensible heat flux anomaly of 4 W m^{-2} , respectively, under the January climatological wind speed over the Caribbean Sea.

c. Moisture balance over the Caribbean Sea

Associated with the humidity variation in the boundary layer, we expect changes in the hydrological processes. To see the changes, we diagnose a vertical integrated moisture budget equation as follows:

$$E'_{est} = \frac{1}{g} \int_{300}^{P_s} \nabla \cdot (q\mathbf{V})' dp + P', \quad (4)$$

where P_s is the pressure surface, \mathbf{V} is the horizontal component of the velocity vector, P is the precipitation, and E is the evaporation from the ocean surface. As a result, Eq. (4) indicates that a change in evaporation is diagnostically determined by changes in atmospheric hydrological processes: the moisture flux anomaly divergence and the precipitation anomaly. This diagnostic equation does not necessary mean that the terms on the right-hand side are always independent of each other.

When we use the precipitation anomaly of CMAP (P'_{CMAP}) and the moisture flux anomaly divergence of NCEP2 ($\nabla \cdot (q\mathbf{V})'$), E'_{est} is in good agreement with the evaporation of NCEP2 (E') in January during the ENSO warm events (Fig. 11a). Due to the small precipitation anomaly during that time, the negative anomaly of the moisture flux divergence nearly balances the suppressed evaporation, which is consistent with the positive q'_a over the Caribbean region (Fig. 8a). Using the precipitation based on NCEP2 instead of CMAP, this

Fig. 11

anomalous moisture flux convergence still contributes to the suppressed surface evaporation (Fig. 11b), and can be mainly explained by the contribution of anomalous wind convergence ($-\nabla \cdot (q\mathbf{V})' \approx -\bar{q}\nabla \cdot \mathbf{V}'$), as described below. Over the Caribbean region, the anomalous moisture transport is represented by the product of anomalous wind and climatological specific humidity ($\nabla \cdot (q\mathbf{V})' \approx \nabla \cdot (\bar{q}\mathbf{V}')$) because the ratio of the anomaly to the climatology in winds is greater than that in specific humidity ($\mathbf{V}'/\bar{\mathbf{V}} \sim 10^{-1}$ and $q'/\bar{q} \sim 10^{-2}$). In addition, the anomalous wind advection is relatively small (i.e., $\nabla \cdot (\bar{q}\mathbf{V}') \approx \bar{q}\nabla \cdot \mathbf{V}'$) because the climatological specific humidity is almost uniform around the Caribbean Sea. During the ENSO warm events, surface northwesterly from the Gulf of Mexico and southerly from the South America that may be induced by the ENSO forcing tend to converge over the Caribbean region (Fig. 2h). These results suggest that the suppressed surface evaporation balances the anomalous moisture flux convergence induced by surface wind anomaly convergence.

5. Summary

We showed, during the ENSO events, that latent heat flux anomalies in January are the major contributors in forming SSTAs over the Caribbean Sea (Figs. 2 and 3). Over this region, the calculation of linearized components of latent heat flux anomalies indicated that an anomalous air-sea difference in specific humidity ($\Delta q'$), rather than a wind speed anomaly (W'), plays an important role in generating substantial latent heat flux anomalies after the mature phases of the ENSO events. Specifically, the contribution of $\Delta q'$ during the ENSO warm events accounts for 64% of total latent heat flux anomaly in January over the Caribbean region (Fig. 4).

As mentioned in Section 1, many observational and modeling studies have indicated that

W' is necessary to the substantial latent heat flux anomalies for forming SSTAs over the NTA regions during the ENSO events. On the other hand, model experiments conducted by Saravanan and Chang (2000) suggested the relative importance of $\Delta T'$ in generating latent heat flux anomalies. Our composite and correlation analyses for the observational datasets indicated that, in addition to the W' , the $\Delta q'$ plays an important role in generating latent heat flux anomalies over the Caribbean region particularly during the ENSO warm events.

The correlation analysis showed that the $\Delta q'$ over the Caribbean Sea, compared to the W' , is significantly correlated with the Niño3 index (Fig. 7). Specifically, the scatter plots of $\Delta q'$ showed the strong negative correlation with the positive Niño3 index (Fig. 7b). The January composite maps during the ENSO warm events indicated that the negative $\Delta q'$ over the Caribbean Sea is collocated with the positive q'_a (Fig. 8). Since SSTA over this region is small (Fig. 2b), this positive q'_a should be formed by atmospheric processes. Associated with this positive q'_a over the Caribbean region, positive temperature anomalies at 400 hPa appear over this region extending from eastern tropical Pacific (Fig. 9), which is consistent with the TT-mechanism (Chiang and Sobel 2002). Our diagnosis of a moisture budget equation indicated that the suppressed evaporation nearly balances the anomalous moisture flux convergence (Fig. 11a).

Acknowledgments. The authors are grateful to Profs. M. Ikeda, K. Yamazaki, A. Kubokawa, and M. Watanabe for their stimulating discussions. The manuscript benefitted from the constructive comments by Prof. S.-P. Xie and anonymous reviewers. The NCEP and NCEP2 datasets were provided by the NOAA-CIRES Climate Diagnostics Center, Boulder, Colorado, USA, from their website (at <http://www.cdc.noaa.gov/>). This work was partly supported by Grand-In-Aid for Scientific Research defrayed by the Ministry of Education,

Culture, Sports, Science and Technology of Japan (15540416) and by Category 7 of the MEXT RR 2002 Project for Sustainable Coexistence of Human, Nature and the Earth.

REFERENCES

- Alexander, M. A., and J. D. Scott, 2002: The influence of ENSO on air-sea interaction in the Atlantic. *Geophys. Res. Lett.*, **29**, 46, doi:10.1029/2001GL014347.
- Brown, R. G., and C. S. Bretherton, 1997: A test of the strict quasi-equilibrium theory on long time and space scales. *J. Atmos. Sci.*, **54**, 624–638.
- Carton, J. A., and Z. Zhou, 1997: Annual cycle of sea surface temperature in the tropical Atlantic Ocean. *J. Geophys. Res.*, **102**, 27813–27824.
- Charney, J. G., 1963: A note on large-scale motions in the tropics. *J. Atmos. Sci.*, **20**, 607–609.
- Chiang, J. C. H., and A. H. Sobel, 2002: Tropical tropospheric temperature variations caused by ENSO and their influence on the remote tropical climate. *J. Climate*, **15**, 2616–2631.
- Curtis, S., and S. Hastenrath, 1995: Forcing of anomalous sea surface temperature evolution in the tropical Atlantic during Pacific warm events. *J. Geophys. Res.*, **100**, 15835–15847.
- Deweaver, E., and S. Nigam, 2002: Linearity in ENSO’s atmospheric response. *J. Climate*, **15**, 2446–2461.
- Emanuel, K. A., J. D. Neelin, and C. S. Bretherton, 1994: On large-scale circulations in convecting atmospheres. *Quart. J. Roy. Meteor. Soc.*, **120**, 1111–1143.
- Enfield, D. B., and D. A. Mayer, 1997: Tropical Atlantic sea surface temperature variability and its relation to El Niño-Southern Oscillation. *J. Geophys. Res.*, **102**, 929–945.
- Folland, C. K., and D. E. Parker, 1995: Correction of instrumental biases in historical sea surface temperature data. *Quart. J. Roy. Meteor. Soc.*, **121**, 319–367.

- Giannini, A., Y. Kushnir, and M. A. Cane, 2000: Interannual variability of Caribbean rainfall, ENSO, and the Atlantic ocean. *J. Climate*, **13**, 297–311.
- Hoerling, M. P., A. Kumar, and M. Zhong, 1997: El Niño, La Niña, and the nonlinearity of their teleconnections. *J. Climate*, **10**, 1769–1786.
- , ———, and T. Xu, 2001: Robustness of the nonlinear climate response to ENSO’s extreme phases. *J. Climate*, **15**, 1277–1293.
- Huang, B., P. S. Schopf, and Z. Pan, 2002: The ENSO effect on the tropical Atlantic variability: a regionally coupled model study. *Geophys. Res. Lett.*, **29**, 2039, doi:10.1029/2002GL014872.
- Kalnay, E., M. Kanamitsu, R. Kistler, W. Collins, D. Deaven, L. Gandin, M. Iredell, S. Saha, G. White, J. Wollen, Y. Zhu, M. Chelliah, W. Ebisuzaki, W. Higgins, J. Janowiak, K. C. Mo, C. Ropelewski, J. Wang, A. Leetmaa, R. Reynolds, R. Jenne, and D. Joseph, 1996: The NCEP/NCAR 40-year reanalysis project. *Bull. Amer. Meteor. Soc.*, **77**, 437–471.
- Kanamitsu, M., W. Ebisuzaki, J. Woollen, S.-K. Yang, J. J. Hnilo, M. Fiorino, and G. L. Potter, 2002: NCEP-DOE AMIP-II reanalysis (R-2). *Bull. Amer. Meteor. Soc.*, **83**, 1631–1643.
- Kara, A. B., P. A. Rochford, and H. E. Hurlburt, 2003: Mixed layer depth variability over the global ocean. *J. Geophys. Res.*, **108**, doi:10.1029/2000JC000736.
- Kleeman, R., G. Wang, and S. Jewson, 2001: Surface flux response to interannual tropical Pacific sea surface temperature variability in AMIP models. *Clim. Dyn.*, **17**, 627–641.
- Klein, S. A., B. J. Soden, and N. C. Lau, 1999: Remote sea surface temperature variations during ENSO: evidence for a tropical atmospheric bridge. *J. Climate*, **12**, 917–932.
- Lau, N. C., and M. J. Nath, 2001: Impact of ENSO on SST variability in the North Pacific

- and North Atlantic: seasonal dependence and role of extratropical air-sea coupling. *J. Climate*, **14**, 2846–2866.
- Liu, Z., Q. Zhang, and L. Wu, 2004: Remote impact on tropical Atlantic climate variability: statistical assessment and dynamic assessment. *J. Climate*, **17**, 1529–1549.
- Mo, K. C., and R. W. Higgins, 1996: Large-scale atmospheric moisture transport as evaluated in the NCEP/NCAR and the NASA/DAO reanalyses. *J. Climate*, **9**, 1531–1545.
- Okumura, Y., and S. P. Xie, 2004: Interaction of the Atlantic equatorial cold tongue and African monsoon. *J. Climate*, **17**, 3588–3601.
- , ——, A. Numaguti, and Y. Tanimoto, 2001: Tropical Atlantic air-sea interaction and its influence on the NAO. *Geophys. Res. Lett.*, **28**, 1507–1510.
- Rajagopalan, B., Y. Kushnir, and Y. Tourre, 1998: Observed decadal midlatitude and tropical Atlantic climate variability. *Geophys. Res. Lett.*, **25**, 3967–3970.
- Saravanan, R., and P. Chang, 2000: Interaction between tropical Atlantic variability and El Niño-Southern oscillation. *J. Climate*, **13**, 2177–2194.
- Smith, T. M., R. W. Reynolds, R. E. Livezey, and D. C. Stokes, 1996: Reconstruction of historical sea surface temperatures using empirical orthogonal functions. *J. Climate*, **9**, 1403–1420.
- Sobel, A. H., I. M. Held, and C. S. Bretherton, 2002: The ENSO signal in tropical tropospheric temperature. *J. Climate*, **15**, 2702–2706.
- Sutton, R. T., S. P. Jewson, and D. P. Rowell, 2000: The elements of climate variability in the tropical Atlantic region. *J. Climate*, **15**, 3261–3284.

- Tanimoto, Y., and S. P. Xie, 1999: Ocean-atmosphere variability over the pan-Atlantic basin. *J. Meteor. Soc. Japan*, **77**, 31–46.
- , and ——, 2002: Inter-hemisphere decadal variations in SST, surface wind, heat flux and cloud cover over the Atlantic ocean. *J. Meteor. Soc. Japan*, **80**, 1199–1219.
- , H. Nakamura, T. Kagimoto, and S. Yamane, 2003: An active role of extratropical sea surface temperature anomalies in determining anomalous turbulent heat flux. *J. Geophys. Res.*, **108**, 3304, doi:10.1029/2002JC001750.
- Toure, Y., B. Rajagopalan, and Y. Kushnir, 1999: Dominant patterns of climate variability in the Atlantic ocean region during the last 136 years. *J. Climate*, **12**, 2285–2299.
- Trenberth, K. E., and C. J. Guillemot, 1995: Evaluation of the global atmospheric moisture budget as seen from analyses. *J. Climate*, **8**, 2255–2272.
- , and ——, 1998: Evaluation of the atmospheric moisture and hydrological cycle in the NCEP/NCAR reanalyses. *Clim. Dyn.*, **14**, 213–231.
- Wallace, J. M., 1992: Effect of deep convection on the regulation of tropical sea surface temperature. *Nature*, **357**, 230–231.
- Wang, C., 2002: Atlantic climate variability and its associated atmospheric circulation cells. *J. Climate*, **15**, 1516–1536.
- Woodruff, S. D., R. J. Slutz, R. L. Jenne, and P. M. Steurer, 1987: A comprehensive ocean-atmosphere data set. *Bull. Amer. Meteor. Soc.*, **68**, 1239–1250.
- Xie, P., and P. A. Arkin, 1997: Global precipitation: a 17-year monthly analysis based on gauge observations, satellite estimates, and numerical model outputs. *Bull. Amer. Meteor. Soc.*, **78**, 2539–2558.
- Xie, S. P., and J. A. Carton, 2004: Tropical Atlantic variability: patterns, mechanisms, and

- impacts. *Earth Climate: Ocean-atmosphere interaction and climate variability*, **147**, 121–142, Geophysical Monograph, AGU, Washington D. C.
- , and S. G. H. Philander, 1994: A coupled ocean-atmosphere model of relevance to the ITCZ in the eastern Pacific. *Tellus*, **46A**, 340–350.
- , and Y. Tanimoto, 1998: A pan-Atlantic decadal climate oscillation. *Geophys. Res. Lett.*, **25**, 2185–2188.
- Yulaeva, E., and J. M. Wallace, 1994: The signature of ENSO in global temperature and precipitation fields derived from the microwave sounding unit. *J. Climate*, **7**, 1719–1736.
- Zebiak, S. E., 1993: Air-sea interaction in the equatorial Atlantic region. *J. Climate*, **6**, 1567–1586.

Captions of Figures

FIG. 1. Niño3 index (unit: °C) averaged from November to January in the following year. White (black) bars denote the eight ENSO warm (cold) events.

FIG. 2. Monthly composite maps of SSTAs (left panels), SSTA tendencies (center panels), latent heat flux anomalies (contours in right panels), and surface wind anomalies (arrows in right panels) in December (top), January (middle), and February (bottom) during the ENSO warm events. Contour intervals are 0.2 °C in the left panels, 0.1 °C/2-month in the center panels, and 7.5 W m⁻² (positive anomalies indicate heat loss from the ocean) in the right panels. Zero contours are omitted. The reference vector at the upper right corner indicates 2 m s⁻¹. An SSTA tendency in a given month is defined by the difference between the SSTA in the subsequent month and that in the previous one. These variables are based on NCEP-NCAR reanalysis and GISST.

FIG. 3. Same as in Fig. 2, but for ENSO cold events.

FIG. 4. Composites of (a,e) contributions from W' , (b,f) contributions of $\Delta q'$, (c,g) the sum of these contributions (bars) to the total amount of latent heat flux anomalies (dashed lines), and (d,h) the net heat flux anomalies (bars) averaged over the Caribbean Sea (the rectangular region: 10 - 20 ° N and 80 - 60 ° W) during the ENSO warm (left panels) and cold (right panels) events based on NCEP-NCAR reanalysis and GISST. The total amount of latent heat flux anomalies (dashed lines) and SSTA (solid line; right axis) are superimposed on (d) and (h). White (black) bars denote negative (positive) anomalies. Units in left (right) axis are W m⁻² (°C).

FIG. 5. January composite maps of (a,d) contributions from wind speed anomaly (W'), (b,e) contributions of anomalous air-sea difference in specific humidity ($\Delta q'$), and (c,f)

the sum of these contributions during the ENSO warm events. Left (right) panels are derived from NCEP-NCAR reanalysis and GISST datasets (COADS). Contour intervals are 5 W m^{-2} (upper and middle panels) and 7.5 W m^{-2} (bottom panels). Zero contours are omitted.

FIG. 6. Same as in Fig. 5, but for ENSO cold events.

FIG. 7. January scatter plots of (a) the wind speed anomaly (m s^{-1}), (b) the anomalous air-sea difference in specific humidity (g kg^{-1}), and (c) the specific humidity anomaly at 2-m (g kg^{-1}) over the Caribbean Sea onto the Niño3 index (x-axis; $^{\circ}\text{C}$). Solid circles indicate the eight warm and cold events. Values at the center above the panels indicate the correlation coefficients calculated from all scatter plots. Values at the left (right) corner above the panels indicate the correlation coefficients calculated from scatter plots only during negative (positive) phase of the Niño3 index. A correlation coefficient of 0.44 is statistically significant at 95% level under 20 degrees of freedom.

FIG. 8. January composite maps of (a) q'_a and (b) $\Delta q'$ during the ENSO warm events. Contour intervals are 0.2 g kg^{-1} . Zero contours are omitted.

FIG. 9. January composite map of temperature anomaly at 400 hPa based on NCEP-NCAR reanalysis during the ENSO warm events. Contour intervals are $0.5 \text{ }^{\circ}\text{C}$. Zero contours are omitted.

FIG. 10. Composites of air temperature anomaly at 2-m (thick solid line; $^{\circ}\text{C}$) and SSTA (dashed line; $^{\circ}\text{C}$) over the Caribbean Sea derived from (a) NCEP-NCAR reanalysis and GISST and (b) COADS during the ENSO warm events. Thin solid line plotted with each panels is the air temperature anomalies at 400 hPa in NCEP-NCAR reanalysis divided by 2.

FIG. 11. January moisture budget in the Caribbean Sea during the warm events using precipitation based on (a) CMAP and (b) NCEP2. All other variables are based on NCEP2. In these datasets, we take 5 years for the composite during the ENSO warm events.

Caption of Table

TABLE 1. Years of ENSO warm and cold events.

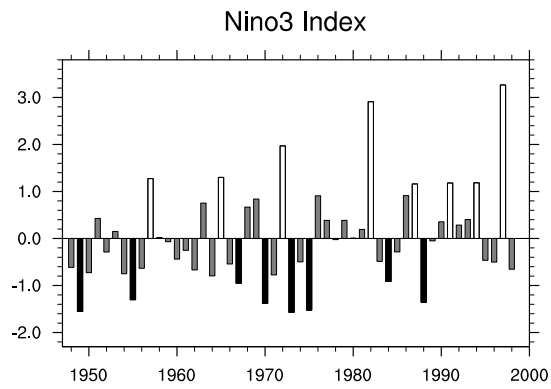


FIG. 1. Niño3 index (unit: °C) averaged from November to January in the following year. White (black) bars denote the eight ENSO warm (cold) events.

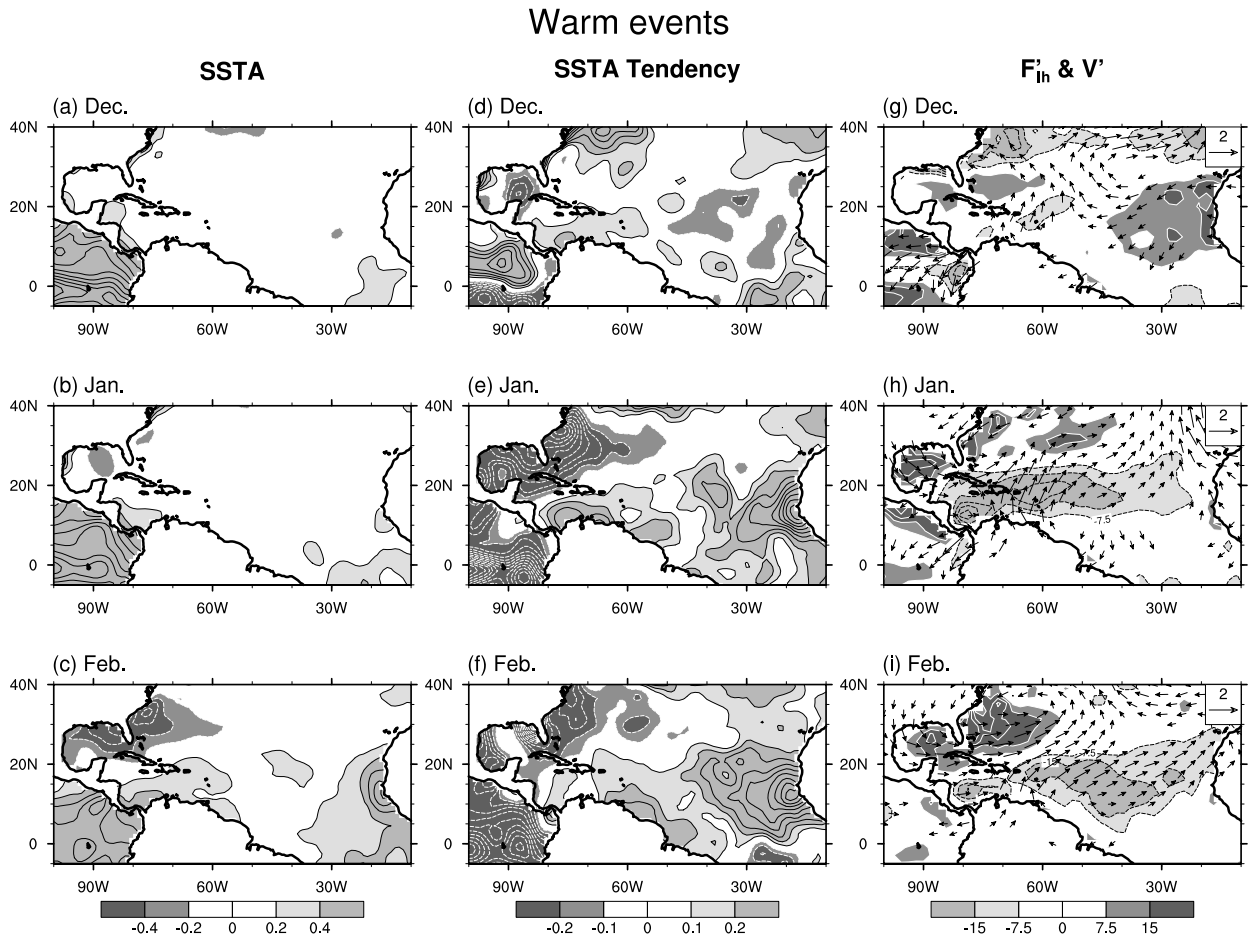


FIG. 2. Monthly composite maps of SSTAs (left panels), SSTA tendencies (center panels), latent heat flux anomalies (contours in right panels), and surface wind anomalies (arrows in right panels) in December (top), January (middle), and February (bottom) during the ENSO warm events. Contour intervals are $0.2\text{ }^{\circ}\text{C}$ in the left panels, $0.1\text{ }^{\circ}\text{C}/2\text{-month}$ in the center panels, and 7.5 W m^{-2} (positive anomalies indicate heat loss from the ocean) in the right panels. Zero contours are omitted. The reference vector at the upper right corner indicates 2 m s^{-1} . An SSTA tendency in a given month is defined by the difference between the SSTA in the subsequent month and that in the previous one. These variables are based on NCEP-NCAR reanalysis and GISST.

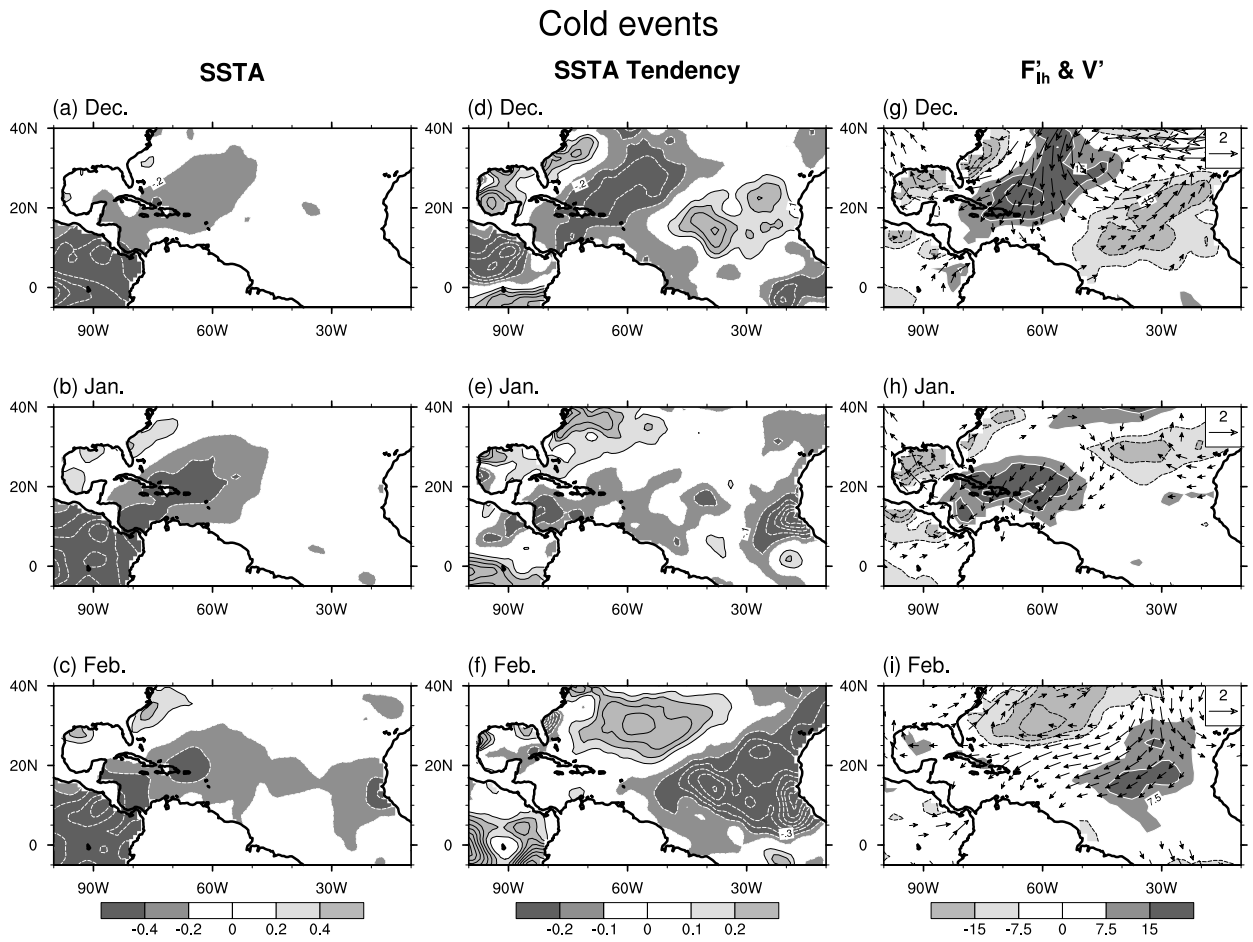


FIG. 3. Same as in Fig. 2, but for ENSO cold events.

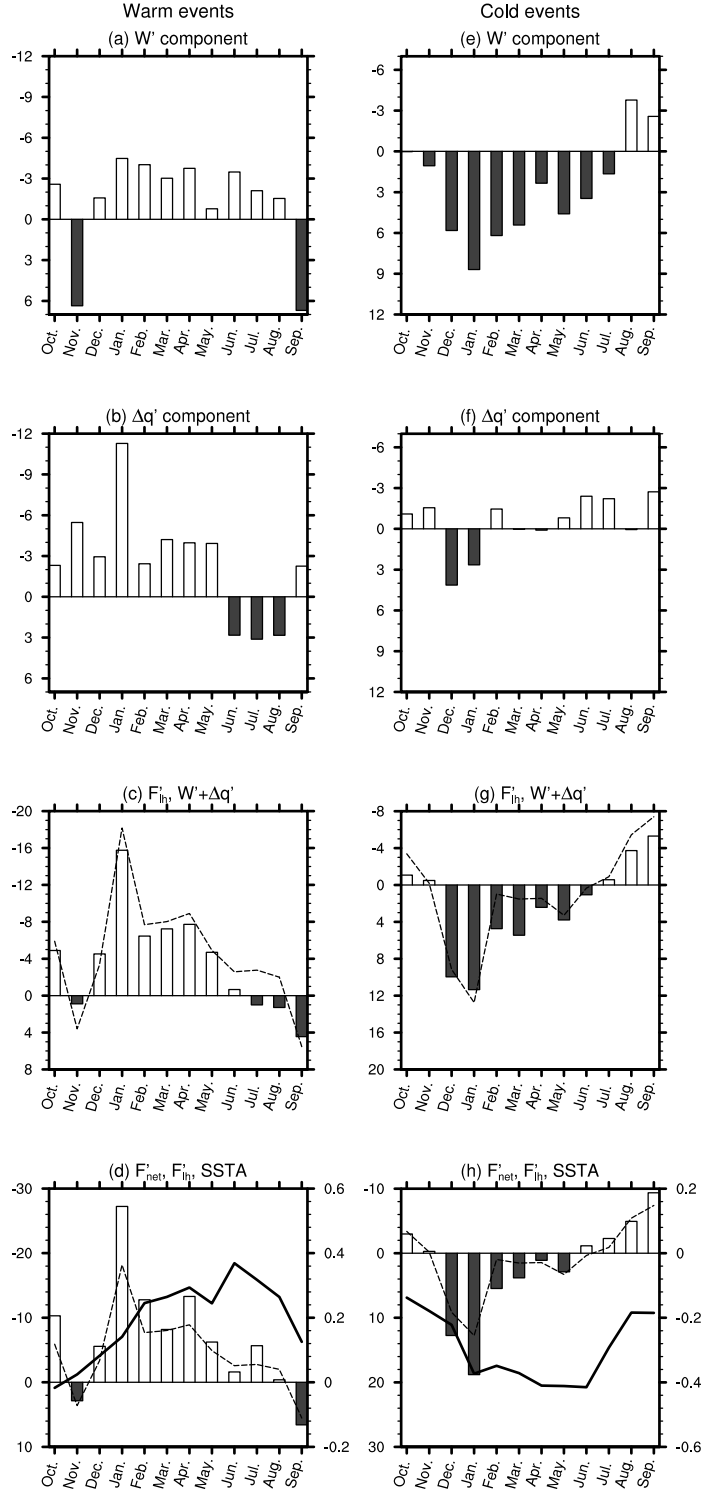


FIG. 4. Composites of (a,e) contributions from W' , (b,f) contributions of $\Delta q'$, (c,g) the sum of these contributions (bars) to the total amount of latent heat flux anomalies (dashed lines), and (d,h) the net heat flux anomalies (bars) averaged over the Caribbean Sea (the rectangular region: $10 - 20^\circ \text{N}$ and $80 - 60^\circ \text{W}$) during the ENSO warm (left panels) and cold (right panels) events based on NCEP-NCAR reanalysis and GISST. The total amount of latent heat flux anomalies (dashed lines) and SSTA (solid line; right axis) are superimposed on (d) and (h). White (black) bars denote negative (positive) anomalies. Units in left (right) axis are W m^{-2} ($^\circ \text{C}$).

(IV)

Warm events (Jan.)

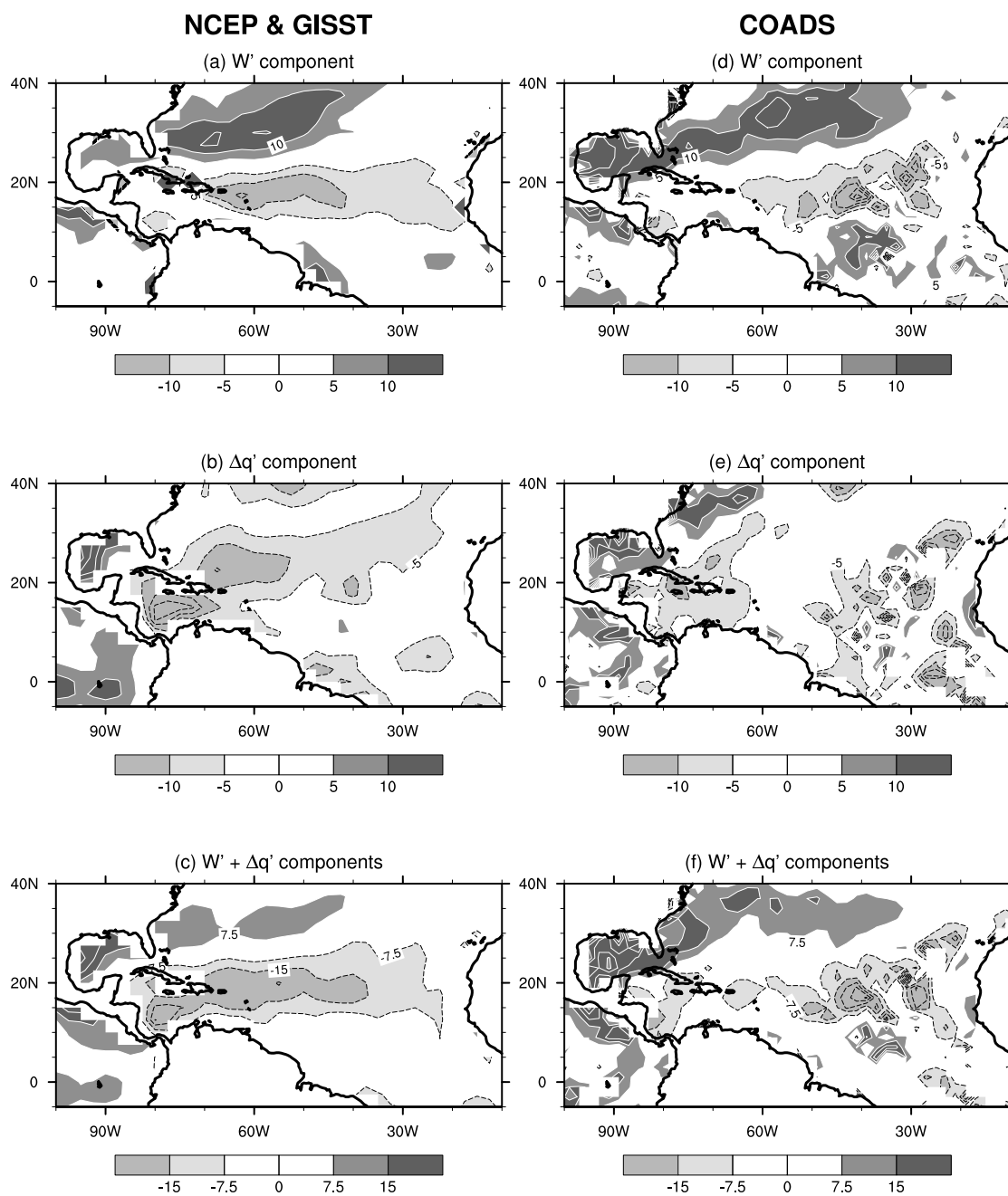


FIG. 5. January composite maps of (a,d) contributions from wind speed anomaly (W'), (b,e) contributions of anomalous air-sea difference in specific humidity ($\Delta q'$), and (c,f) the sum of these contributions during the ENSO warm events. Left (right) panels are derived from NCEP-NCAR reanalysis and GISST datasets (COADS). Contour intervals are 5 W m^{-2} (upper and middle panels) and 7.5 W m^{-2} (bottom panels). Zero contours are omitted.

Cold events (Jan.)

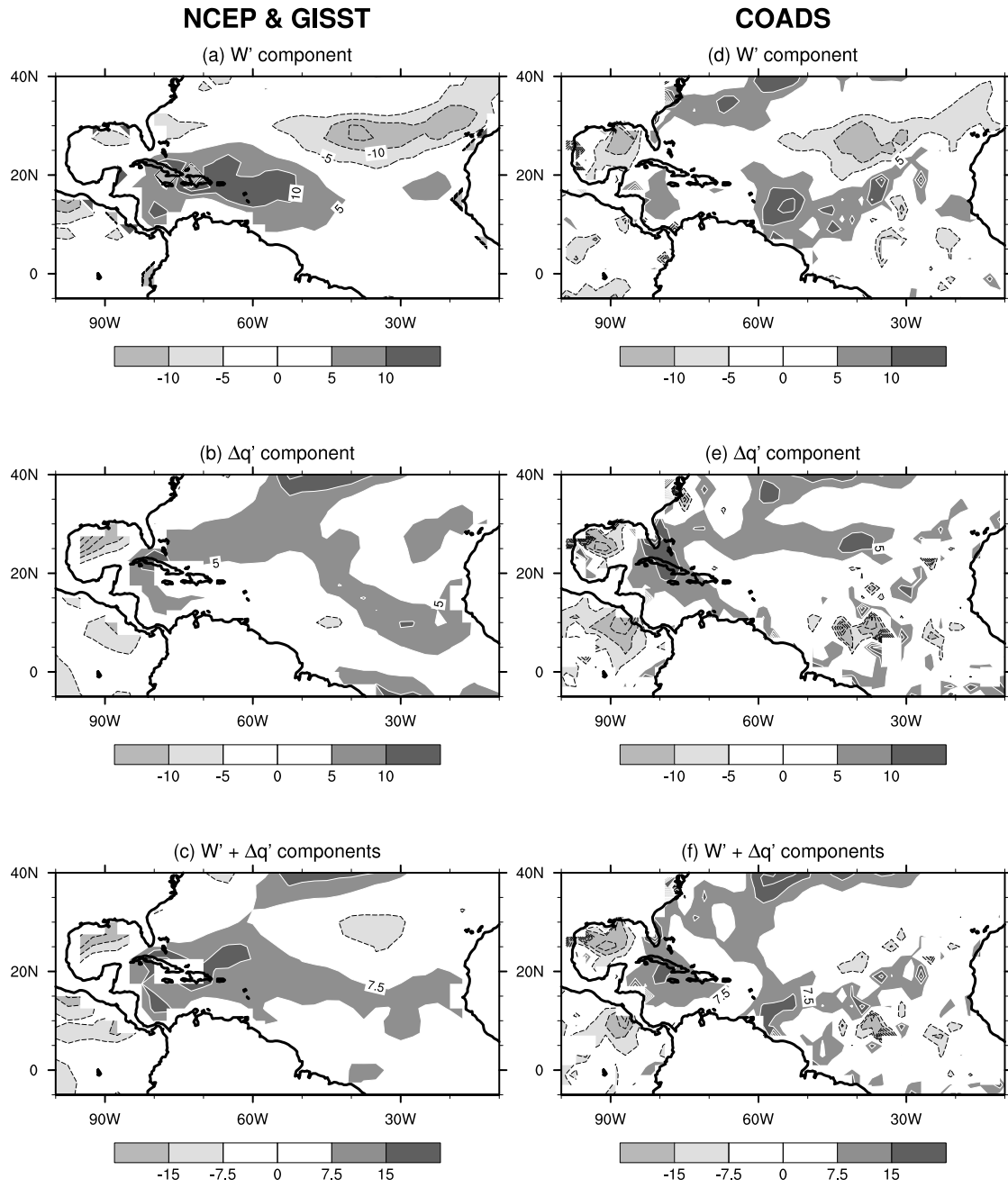


FIG. 6. Same as in Fig. 5, but for ENSO cold events.

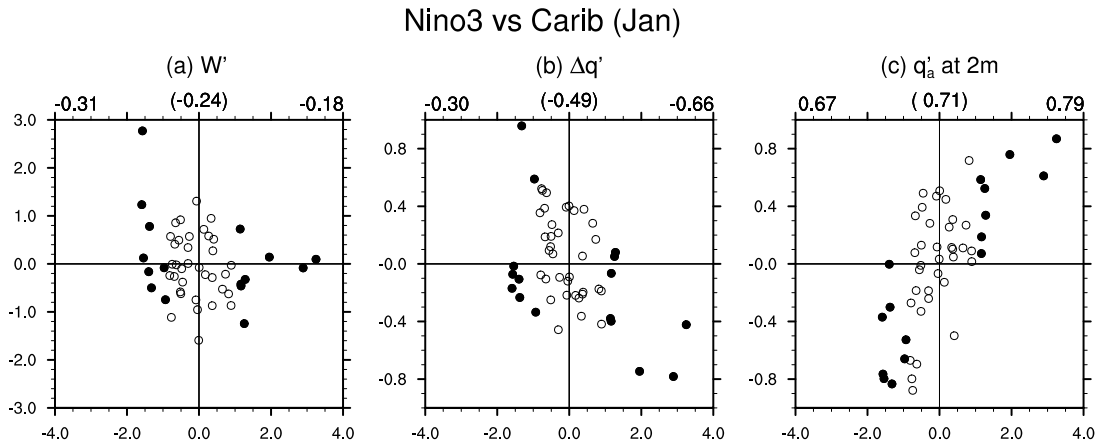


FIG. 7. January scatter plots of (a) the wind speed anomaly (m s^{-1}), (b) the anomalous air-sea difference in specific humidity (g kg^{-1}), and (c) the specific humidity anomaly at 2-m (g kg^{-1}) over the Caribbean Sea onto the Niño3 index (x-axis; $^{\circ}\text{C}$). Solid circles indicate the eight warm and cold events. Values at the center above the panels indicate the correlation coefficients calculated from all scatter plots. Values at the left (right) corner above the panels indicate the correlation coefficients calculated from scatter plots only during negative (positive) phase of the Niño3 index. A correlation coefficient of 0.44 is statistically significant at 95% level under 20 degrees of freedom.

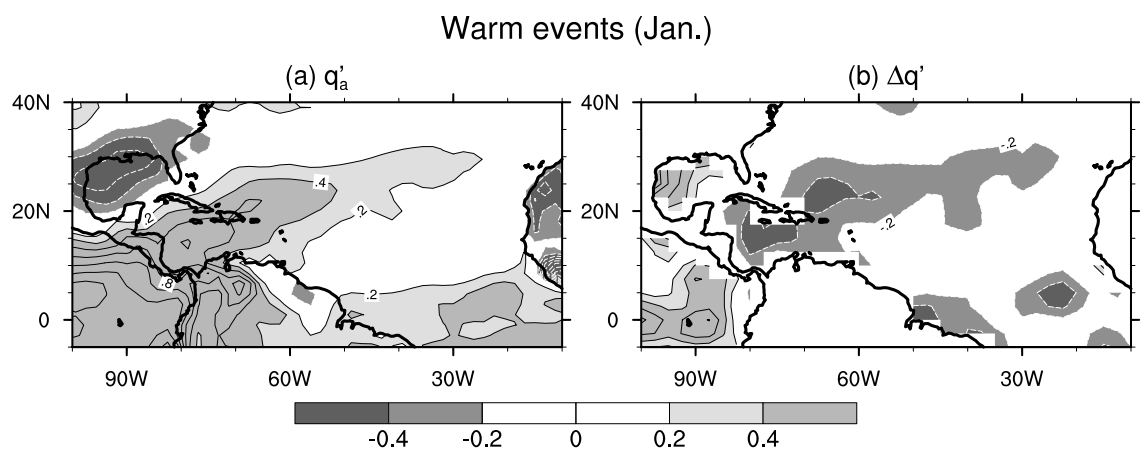


FIG. 8. January composite maps of (a) q'_a and (b) $\Delta q'$ during the ENSO warm events. Contour intervals are 0.2 g kg^{-1} . Zero contours are omitted.

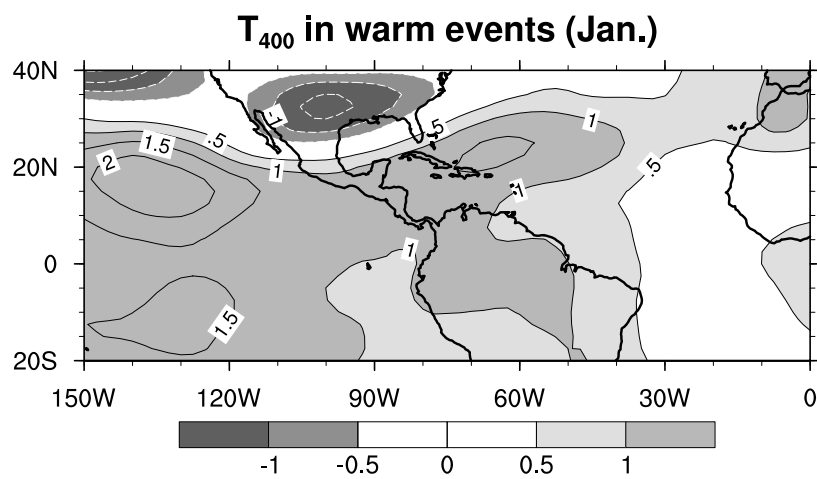


FIG. 9. January composite map of temperature anomaly at 400 hPa based on NCEP-NCAR reanalysis during the ENSO warm events. Contour intervals are 0.5 °C. Zero contours are omitted.

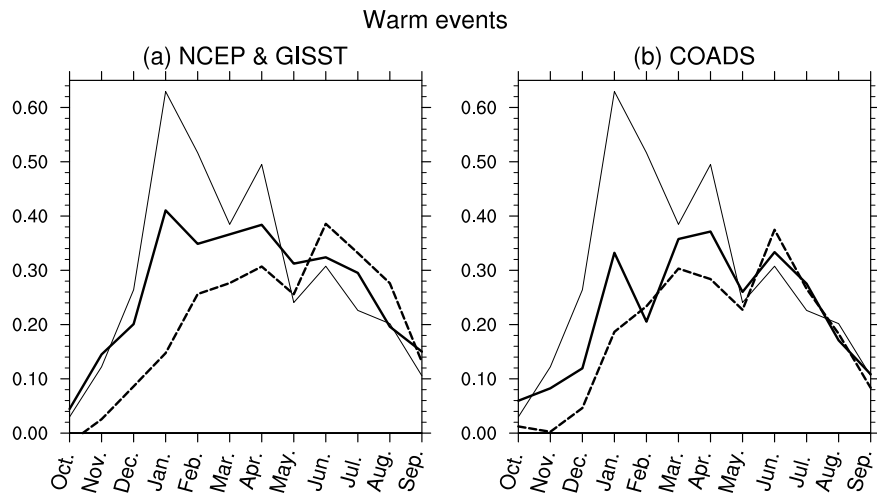


FIG. 10. Composites of air temperature anomaly at 2-m (thick solid line; $^{\circ}\text{C}$) and SSTA (dashed line; $^{\circ}\text{C}$) over the Caribbean Sea derived from (a) NCEP-NCAR reanalysis and GISST and (b) COADS during the ENSO warm events. Thin solid line plotted with each panels is the air temperature anomalies at 400 hPa in NCEP-NCAR reanalysis divided by 2.

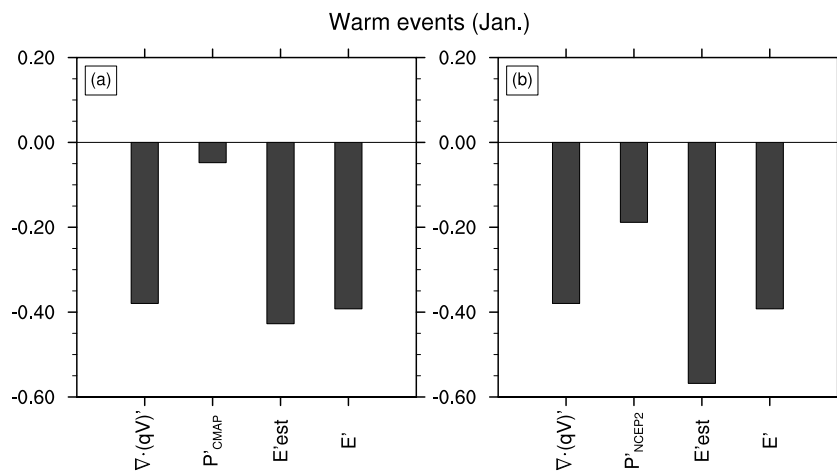


FIG. 11. January moisture budget in the Caribbean Sea during the warm events using precipitation based on (a) CMAP and (b) NCEP2. All other variables are based on NCEP2. In these datasets, we take 5 years for the composite during the ENSO warm events.

TABLE 1. Years of ENSO warm and cold events.

Warm events	Cold events
1957/58	1949/50
1965/66	1955/56
1972/73	1967/68
1982/83	1970/71
1987/88	1973/74
1991/92	1975/76
1994/95	1984/85
1997/98	1988/89